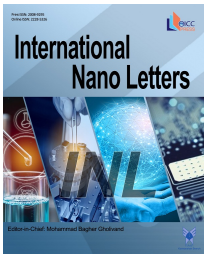

Volume 15, Issue 4, 152513 (1-10)

International Nano Letters (INL)

https://doi.org/10.57647/inl.2025.1504.13

Luminescent $ZnWO_4$:Ag Fibers as Flexible Platforms for Smart Radiation Sensitive Textiles

Sanaz Alamdari[1,*], Amir Hossein Jabbar Sadooni[2], Somayeh Salmani Shik[2]

[1] *Department of Nanotechnology, Faculty of New Sciences and Technologies, Semnan University, Semnan, Iran.*
[2] *Photonics Laboratory, Department of Physics, Kharazmi University, Alborz, Iran.*

[*] **Corresponding authors:** s.alamdari@semnan.ac.ir

Original Research

Received:
4 August 2025
Revised:
9 November 2025
Accepted:
21 November 2025
Published online:
30 December 2025

Abstract:

In this study, Ag-doped $ZnWO_4$ fibers were successfully fabricated using a simple, low-cost drawing technique, and their structural, morphological, and optical properties were systematically investigated, with particular emphasis on their response to ionizing radiation. $ZnWO_4$ and $ZnWO_4$:Ag nanopowders were first synthesized via a coprecipitation method and subsequently embedded into a polymeric matrix to form flexible microfibers. X-ray diffraction (XRD) analysis confirmed the formation of a single-phase monoclinic wolframite $ZnWO_4$ structure, while Ag incorporation induced slight peak shifting and reduced crystallinity due to lattice distortion. Raman spectroscopy further verified the preservation of characteristic WO_4^{2-} vibrational modes. FESEM observations revealed the successful formation of continuous microfibers with average diameters of approximately 12 µm for pristine $ZnWO_4$ fibers and 15 µm for Ag-doped fibers, with uniformly distributed Ag nanoparticles decorating the fiber surface, as confirmed by EDS and elemental mapping analyses. Optical studies demonstrated a strong emission band centered at $\sim$ 500 nm in both photoluminescence (PL) and ion beam induced luminescence (IBIL) spectra. Notably, Ag-doped $ZnWO_4$ fibers exhibited significantly enhanced luminescence intensity compared to undoped samples under both UV excitation and 2.2 MeV proton irradiation, attributed to Ag-induced defect states, improved charge carrier trapping, and enhanced radiative recombination. The IBIL intensity was substantially higher than PL due to the higher excitation efficiency of energetic protons. These findings highlight the strong potential of Ag-doped $ZnWO_4$ nanofibers as advanced functional materials for ionizing radiation detection, scintillation devices, and smart textile applications.

Keywords: Phosphor; $ZnWO_4$; Optical sensitivity; Nanofibers

Cite this article: Alamdari, S., Jabbar Sadooni, A.H., Salmani Shik, S. Luminescent $ZnWO_4$:Ag Fibers as Flexible Platforms for Smart Radiation Sensitive Textiles. *Int. Nano Lett.* **15**(4), 152513 (2025).

1. Introduction

The application of ionizing radiation as a tool for modifying nanofibrous materials has gained increasing attention due to its effectiveness in tailoring material properties at the nanoscale. Ionizing radiation can induce controlled structural transformations, promote crosslinking, and enable surface functionalization, thereby significantly improving the mechanical strength, thermal stability, and chemical resistance of nanofibers. These enhancements expand the applicability of radiation-modified nanofibers across a wide range of fields, including biomedicine, environmental remediation, electronics, and energy-related technologies.

Traditionally, electronic textiles (e-textiles) have been fabricated through the direct incorporation of functional nanoparticles into textile matrices [1–3] or by integrating functional fibers with conventional fibers via weaving, knitting, or embroidery, often forming coaxial or twisted architectures [4]. Within this framework, optically stimulated luminescence (OSL) fibers have emerged as an important class of physical dosimeters for ionizing radiation. These fibers typically rely on wide-bandgap insulating materials and are further enhanced by embedding luminescent semiconductor fillers to improve their radiation sensitivity and optical response. Among various luminescent materials, tungstate-based compounds have attracted considerable interest owing to their outstanding optoelectronic properties, including tunable

bandgaps, high photoluminescence quantum yields, and excellent color purity. Previous studies have reported the successful synthesis and investigation of highly sensitive pure and doped tungstate nanomaterials such as $CdWO_4$, $BaWO_4$, Bi_2WO_4, and $PbWO_4$ in the form of nanopowders and polymer-based composite films incorporating matrices such as PVA, PS, and chitosan [5–8]. These materials demonstrated promising luminescent performance under ionizing radiation. Recent studies have demonstrated a simple in situ growth strategy for fabricating large-area $CsPbBr_3$ nanocrystal films with precise thickness control and good uniformity, offering a scalable alternative to conventional spin-coating and vapor deposition methods. Furthermore, Mg^{2+} ion incorporation was shown to enhance crystallinity and passivate surface defects, leading to a significant improvement in luminescence efficiency and ultraviolet photodetector responsivity [9]. Guo et al. systematically investigated the role of spacer units in bottlebrush block copolymers (BBCPs), demonstrating that spacer length critically governs polymerization efficiency, chain propagation, and self-assembled domain spacing. They showed that a trade-off exists between achieving large backbone degrees of polymerization and rapid domain spacing growth, and proposed semicrystalline BBCP architectures capable of forming hierarchical lamellar photonic structures with tunable nanoscale periodicity [10].

The present study emphasizes the significance of ionizing radiation-responsive nanofibers as advanced functional materials with enhanced structural and optical characteristics. A simple and cost-effective fabrication strategy was employed to produce luminescent nanofibers, and for the first time, their structural features and optical responses were systematically evaluated under ionizing radiation. The findings highlight the potential of these nanofibrous systems for next-generation radiation sensing, smart textiles, and optoelectronic applications.

2. Materials and methods

The main objective of this study was the fabrication of Ag-doped $ZnWO_4$ nanofibers using a simple and cost-effective drawing (pulling) technique, followed by a comprehensive investigation of their structural, morphological, and optical properties. To evaluate the crystalline structure, morphology, and vibrational characteristics of the prepared nanofibers, X-ray diffraction (XRD), scanning electron microscopy (SEM), and Raman spectroscopy analyses were employed.

Materials

All chemical reagents were of analytical grade and used without further purification. The precursor materials required for the synthesis of $ZnWO_4$ nanopowders and nanofibers are listed in Table 1.

Synthesis of $ZnWO_4$ and Ag-Doped $ZnWO_4$ nanopowders

$ZnWO_4$ nanoparticles, both in pristine and Ag-doped forms, can be synthesized using various methods such as coprecipitation, sol–gel, hydrothermal, solvothermal, and solid-state routes. Among these, the coprecipitation method was selected in this study due to its simplicity, low cost, ambient temperature operation, and environmental friendliness, as it does not require surfactants.

For the synthesis of 0.01 mol $ZnWO_4$, equimolar amounts (0.01 mol) of sodium tungstate dihydrate (3.3 g) and zinc acetate dihydrate (2.2 g) were separately dissolved in 5 mL of double-distilled water at room temperature. After complete dissolution, the sodium tungstate solution was added dropwise to the zinc acetate solution under continuous magnetic stirring. Upon mixing, a white precipitate of zinc tungstate formed according to the following reaction:

$$Zn(CH_3CO_2)_2 \cdot 2H_2O(aq) + Na_2WO_4 \cdot 2H_2O(aq) \rightarrow ZnWO_4(s) + 2(Na + CH_3CO_2^-)(aq) + 4H_2O$$

The resulting precipitate was collected and washed four times with double-distilled water and ethanol using centrifugation at 4000 rpm to remove residual impurities. The obtained powder was dried at 80 °C for 12 h, followed by calcination at 600 °C for 2 h to achieve the crystalline $ZnWO_4$ phase.

Ag-doped $ZnWO_4$ nanopowders were synthesized using the same procedure, with an appropriate amount of silver nitrate added to the precursor solution. A schematic illustration of the synthesis steps is presented in figure 1.

Preparation of $ZnWO_4$/Ag nanofibers by the drawing method

$ZnWO_4$/PVA and Ag-doped $ZnWO_4$/PVA composite solutions were prepared separately using a 20:80 weight ratio of inorganic nanoparticles to polymer matrix. After complete dispersion of the $ZnWO_4$ or $ZnWO_4$/Ag powders in the solvent, the solutions were mixed thoroughly in a larger beaker. Poly(vinyl alcohol) was then gradually added to the mixed solutions under continuous magnetic stirring until

Table 1. Raw materials used for the synthesis of $ZnWO_4$/Ag nanofibers.

No.	Chemical name	Chemical formula	Molar mass (g/mol)	Density (g/cm^3)	Purity (%)
1	Zinc acetate dihydrate	$Zn(CH_3COO)_2 \cdot 2H_2O$	219.5	1.735	99.99
2	Sodium tungstate dihydrate	$Na_2WO_4 \cdot 2H_2O$	329.82	4.18	99.99
3	Poly(vinyl alcohol) (PVA)	—	—	—	99.99
4	Silver nitrate	$AgNO_3$	—	—	99.99
5	Double-distilled water	H_2O	18.02	1.0	—

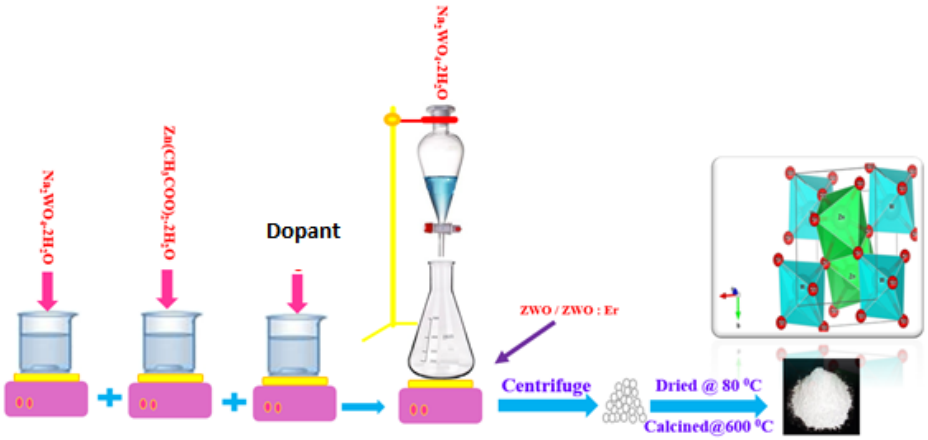

Figure 1. A schematic illustration of the synthesis steps.

a homogeneous and sufficiently viscous solution suitable for fiber drawing was obtained. The prepared solution was subsequently heated to 50 °C using a magnetic stirrer to facilitate solvent evaporation and improve fiber formation. For fiber fabrication, a small amount of the viscous polymeric solution was placed between two metallic plates. The plates were initially brought into contact and then slowly separated, allowing continuous nanofibers to form through the drawing process. The collected fibers were placed on a flat surface and allowed to dry at 50 °C. This procedure was repeated several times to obtain an adequate quantity of nanofibers. Finally, the as-prepared $ZnWO_4$/Ag nanofibers were collected for further characterization. A schematic representation of the drawing process is shown in figure 2, and images of the fabricated samples are presented in figure 3.

Characterization

X-ray diffraction (XRD) analysis was carried out using a Bruker D8 diffractometer equipped with Cu Kα radiation ($\lambda = 1.5406$ Å) to investigate the crystalline structure of the samples. The morphology and size distribution of the nanoparticles were examined by field-emission scanning

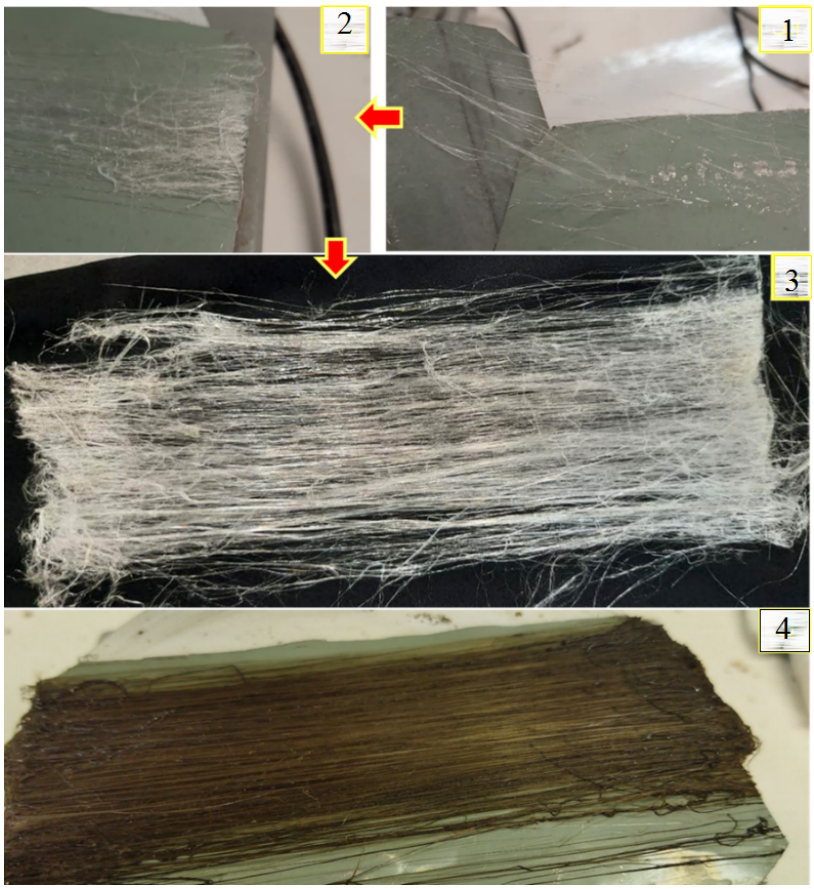

Figure 2. A schematic representation of the drawing process.

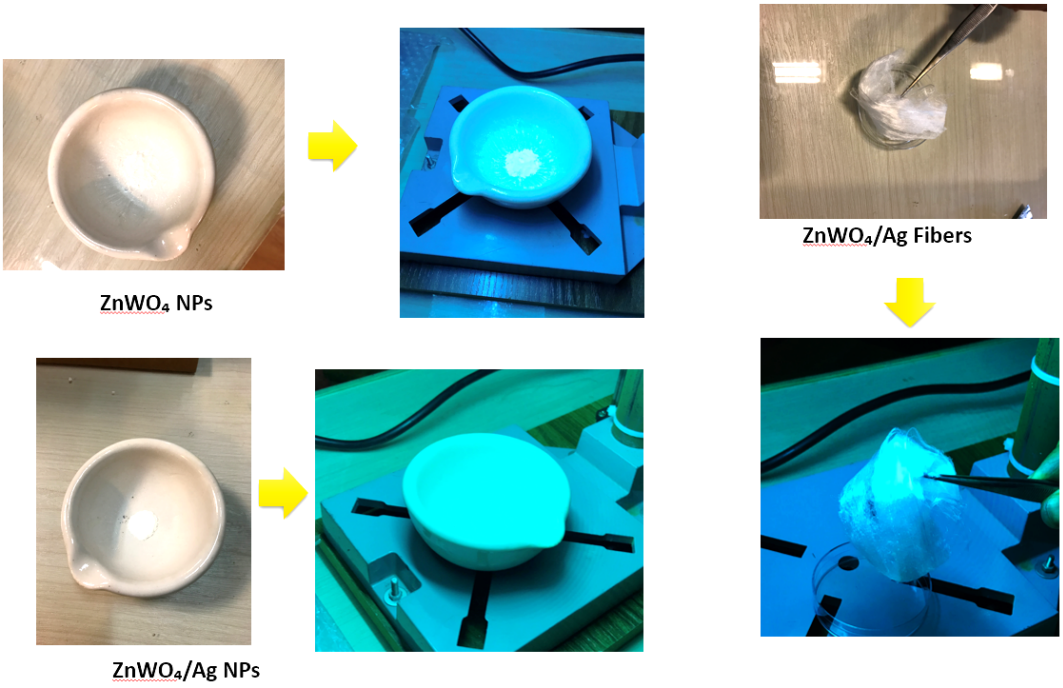

Figure 3. Images of the fabricated samples.

electron microscopy (FE-SEM) using a TESCAN MIRA3 microscope.

Photoluminescence (PL) spectra were recorded using a Varian Cary Eclipse fluorescence spectrophotometer with an excitation wavelength of 290 nm to evaluate the optical emission behavior of the samples. The ion beam–induced luminescence characteristics were studied by irradiating the samples with 2.2 MeV protons using a focused microbeam setup.

To assess the radiation sensitivity of the flexible composite films, the samples were optically coupled to a photomultiplier tube (PMT, Model R1828, Russia) using optical grease. The luminescence count rates were measured under exposure to collimated alpha particles emitted from a ^{241}Am source with an activity of 1 μCi,

3. Results and discussion

Figure 4(a–c) presents the X-ray diffraction (XRD) patterns of pristine $ZnWO_4$ and Ag-doped $ZnWO_4$ in both nanopowder and fibrous forms. As shown in Fig. 4(a), the diffraction peaks of the $ZnWO_4$ nanopowders can be well indexed to the standard monoclinic wolframite structure (JCPDS No. 01 088 0251), confirming the successful formation of a single-phase crystalline $ZnWO_4$ without detectable impurity phases.

Upon Ag doping, the overall diffraction pattern of $ZnWO_4$:Ag nanopowders remains consistent with the parent $ZnWO_4$ structure, indicating that Ag incorporation does not alter the crystal symmetry. However, noticeable changes in peak intensity and peak position are observed. Specifically, several diffraction peaks exhibit reduced intensity and slight broadening, which suggests a decrease in crystallinity and the introduction of lattice strain due to Ag incorporation.

A magnified view of the characteristic diffraction region around $2\theta \approx 30 - 33°$, corresponding mainly to the (111) and (–111) crystallographic planes, is shown in Fig. 4(b). Compared with pristine $ZnWO_4$ nanopowders, the $ZnWO_4$:Ag nanopowders display a clear shift of the diffraction peaks toward lower 2θ angles. This shift indicates an increase in interplanar spacing (d-spacing), which can be attributed to lattice distortion induced by the substitution or incorporation of Ag^+ ions, whose ionic radius is larger than that of Zn^{2+}. Such lattice expansion is commonly associated with dopant-induced strain and defect formation within the host lattice.

Figure 4(c) illustrates the XRD patterns of the fibrous samples ($ZnWO_4$F and $ZnWO_4$:Ag F). Compared to the nanopowder counterparts, the diffraction peaks of the fibrous samples become significantly weaker and broader, indicating a reduction in crystallinity after fiber formation. This behavior is mainly attributed to the presence of the polymeric matrix and the partial amorphization of the inorganic phase during the fiber fabrication process. Moreover, the $ZnWO_4$:Ag fibrous sample exhibits a slight shift toward lower diffraction angles relative to the undoped $ZnWO_4$ fibers, further confirming the successful incorporation of Ag into the $ZnWO_4$ lattice even after fiber processing.

Additionally, the appearance of a broad and weak diffraction halo in the range of $20 - 30°$ in the fibrous samples is associated with the amorphous nature of the polymer and carbonaceous components of the fibers. This feature confirms the formation of a hybrid structure in which crystalline $ZnWO_4$ domains are embedded within an amorphous fibrous matrix.

Overall, the XRD results demonstrate that while the monoclinic crystal structure of $ZnWO_4$ is preserved after Ag doping and fiber fabrication, controlled lattice distortion, reduced crystallinity, and peak shifting are induced. These structural modifications are expected to play a crucial role in

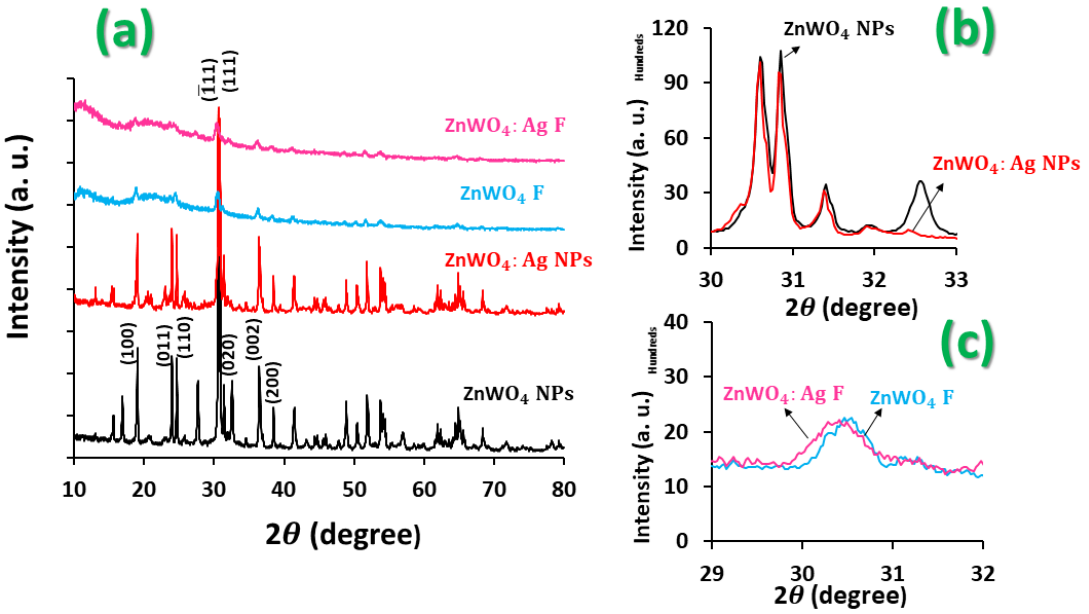

Figure 4. (a–c) XRD patterns of the prepared nanopowders and fiber showing peak intensity variation and peak shift.

enhancing the optical, luminescent, and radiation-sensitive performance of the $ZnWO_4$-based fibrous composites.

Raman spectroscopy analysis

Raman spectroscopy is a powerful and reliable technique for probing the molecular structure, lattice vibrations, and crystallographic properties of materials. This technique is based on the inelastic scattering of incident laser photons by atoms and molecules in a sample, providing detailed information about phonon modes, structural defects, impurity phases, and local lattice distortions. In the case of $ZnWO_4$, Raman spectroscopy is particularly effective for investigating the vibrational modes of WO_4^{2-} groups and assessing the structural integrity of the crystal lattice.

The Raman spectra of the prepared samples are shown in figure 5. In this study, Raman measurements were carried out using a micro-Raman spectrometer (Avantes, model uRaman-532-Ci) equipped with a 532 nm excitation laser. Raman spectroscopy serves as a sensitive tool for identifying intrinsic defects, impurity phases, structural disorder, and oxygen vacancies within the crystal lattice. $ZnWO_4$ crystallizes in a wolframite-type structure, where the lattice is composed of $[WO_4]^{2-}$ tetrahedral units.

According to group theory analysis, the optical phonon modes at the Brillouin zone center (Γ point) for $ZnWO_4$ can be expressed as:

$$\Gamma = 3Ag + 5Au + 5Bg + 3Bu + 5Eg + 5Eu$$

Among these modes, the Ag, Bg, and Eg modes (even parity) are Raman-active, whereas the Au and Eu modes (odd parity) are infrared-active. In addition, the Bu modes are

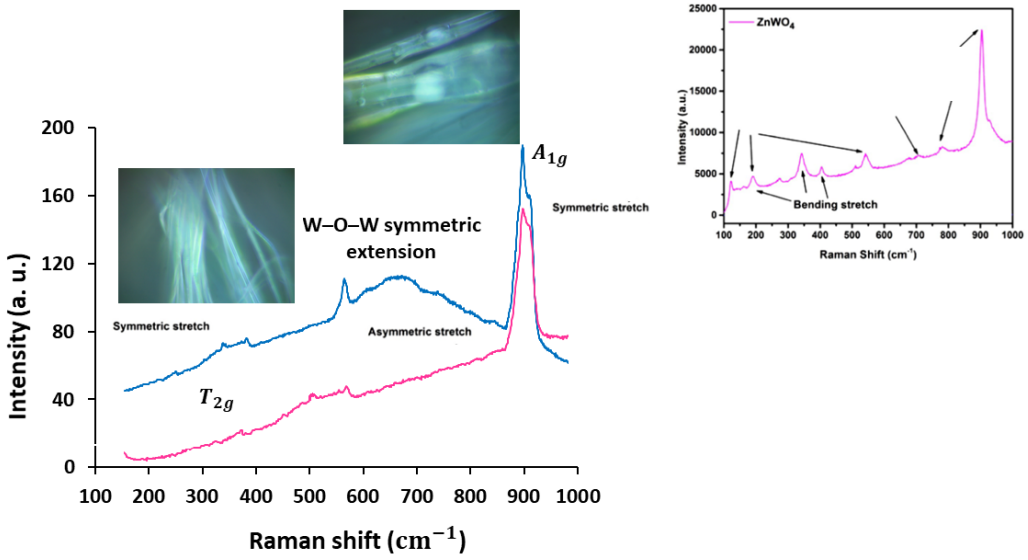

Figure 5. Raman spectra of the prepared fibers.

considered silent modes.

The Raman bands observed at approximately 325 cm^{-1} and 354 cm^{-1} are attributed to the asymmetric bending vibrations of O–W–O bonds. The Raman peaks appearing in the range of $600 - 1000$ cm^{-1} correspond to the stretching vibrations of W–O bonds within the WO_4^{2-} tetrahedra. Specifically, the prominent band centered around 760 cm^{-1} is assigned to the asymmetric stretching mode of W–O bonds, while the strong peak at approximately 904 cm^{-1} is associated with the symmetric stretching vibration of W–O bonds, which is characteristic of the Ag Raman-active mode.

The presence and well-defined nature of these characteristic Raman modes confirm the formation of crystalline $ZnWO_4$ with preserved wolframite structure. Moreover, slight changes in peak position, intensity, or linewidth (if observed) can be associated with lattice distortion, defect formation, or dopant-induced strain, which are consistent with the structural modifications inferred from the XRD analysis.

Overall, the Raman spectroscopy results corroborate the XRD findings and provide further evidence for the successful synthesis of structurally stable $ZnWO_4$-based materials with well-defined vibrational characteristics.

FESEM Analysis of $ZnWO_4$ and $ZnWO_4$:Ag Fibers

Field-emission scanning electron microscopy (FESEM) was employed to investigate the surface morphology, fiber continuity, and the presence and distribution of Ag nanoparticles on the prepared $ZnWO_4$-based fibrous samples. The FESEM images of the fibers at different magnifications are presented in Figs. 6(a–f).

As clearly observed in Figs. 6(a,b), corresponding to the pristine $ZnWO_4$ fibers, the drawing process successfully resulted in the formation of continuous, smooth, and well-defined fibrous structures without noticeable bead formation or structural breakage. The fibers exhibit relatively uniform diameters along their length, indicating good control over the fiber fabrication process. The average diameter of the pristine $ZnWO_4$ fibers was measured to be approximately 12 µm, placing them in the microfibrous regime.

In comparison, the FESEM images of the Ag-doped $ZnWO_4$ fibers shown in Figs. 6(d,e) reveal similarly continuous and homogeneous fibrous morphologies, confirming that Ag incorporation does not disrupt fiber formation. However, a noticeable increase in fiber diameter is observed for the Ag-doped samples, with an average diameter of approximately 15 µm. This increase can be attributed to changes in solution viscosity, nanoparticle–polymer interactions, and structural rearrangements during the drawing process induced by the presence of Ag species.

High-magnification FESEM images (Figs. 6(c,f)) provide further insight into the surface characteristics of the fibers. For the Ag-doped $ZnWO_4$ fibers, numerous bright nanoscale features are observed on the fiber surface, which are attributed to Ag nanoparticles decorating the fibers. These nanoparticles are relatively well dispersed and firmly attached to the fiber surface, indicating effective incorporation and strong interfacial interaction between the Ag nanoparticles and the $ZnWO_4$ fibrous matrix. The uniform decoration of Ag nanoparticles is expected to enhance the functional properties of the fibers, particularly in terms of optical activity, antibacterial performance, and radiation sensitivity.

Overall, the FESEM observations confirm the successful fabrication of continuous $ZnWO_4$ and $ZnWO_4$:Ag mi-

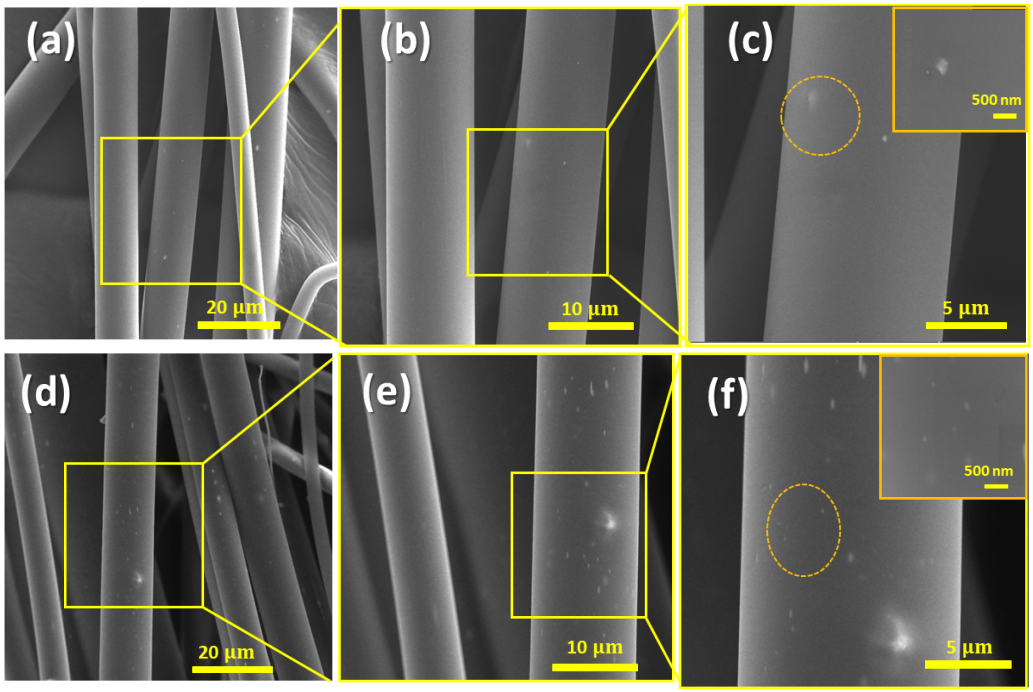

Figure 6. FESEM images of the prepared fibers: (a–c) pristine $ZnWO_4$ fibers at different magnifications, showing continuous microfibrous morphology with smooth surfaces; (d–f) Ag-doped $ZnWO_4$ fibers, revealing increased fiber diameter and uniform surface decoration by Ag nanoparticles (highlighted regions). Scale bars correspond to the indicated magnifications.

crofibers with controlled morphology and effective surface decoration by Ag nanoparticles. The well-preserved fibrous structure and homogeneous nanoparticle distribution provide a favorable microstructural platform for advanced optoelectronic and functional applications.

EDS and elemental mapping analysis

Energy-dispersive X-ray spectroscopy (EDS) and elemental mapping were performed to investigate the elemental composition and spatial distribution of the constituent elements within the $ZnWO_4$:Ag fibrous structure. The corresponding FESEM image and combined elemental maps are presented in Fig. 7(a), while the EDS spectrum and quantitative elemental analysis are shown in Fig. 7(b).

The EDS spectrum confirms the presence of carbon (C), oxygen (O), zinc (Zn), tungsten (W), and silver (Ag) in the analyzed region, verifying the successful formation of the $ZnWO_4$-based fibrous composite and the effective incorporation of Ag species. Quantitative EDS analysis reveals atomic percentages of 66.73% C, 13.16% O, 12.06% Zn, 8.05% W, and 0.90% Ag, as summarized in the inset table of Figure X(b). The high carbon content originates from the PVP polymer matrix, which acts as the fiber-forming medium, while the presence of Zn and W confirms the formation of the $ZnWO_4$ inorganic phase. The detectable Ag content further validates the successful Ag decoration/doping within the fibrous structure.

Elemental mapping images demonstrate a highly uniform spatial distribution of all detected elements along the fiber. The C and O maps exhibit continuous and homogeneous coverage, indicating a well-distributed polymeric and oxide framework throughout the microfiber. Importantly, the Zn and W elemental maps show strong spatial overlap, confirming the homogeneous formation of the $ZnWO_4$ phase without evidence of elemental segregation or secondary-phase-rich regions. The Ag elemental map, despite its relatively low atomic concentration, displays a well-dispersed signal over the fiber surface, indicating that Ag nanoparticles are uniformly distributed rather than forming localized agglomerates.

The combined elemental mapping image further highlights the excellent compositional homogeneity of the $ZnWO_4$:Ag fibers, suggesting effective mixing at the micro- and nanoscale during synthesis and fiber fabrication. Such uniform elemental distribution is highly desirable for ensuring consistent optical performance, antibacterial activity, and radiation-sensitive behavior of the fibrous nanophotocatalyst.

Photoluminescence (PL) spectroscopy

Photoluminescence (PL) spectroscopy was employed to evaluate the fluorescence capability of the synthesized powders, as well as to investigate their potential for ionizing radiation detection and to assess the effect of Ag doping on the optical properties and charge carrier transfer behavior of the $ZnWO_4$ host lattice. For this purpose, the prepared powder samples were irradiated with ultraviolet (UV) light, and their emission responses were systematically examined. As shown in Figure 8, the pristine $ZnWO_4$ powder exhibits a prominent emission peak centered at approximately 498 nm under UV excitation. This emission band lies in the blue–green region of the visible spectrum and is characteristic of $ZnWO_4$-based materials. The Ag-doped $ZnWO_4$ sample displays a noticeably enhanced emission intensity

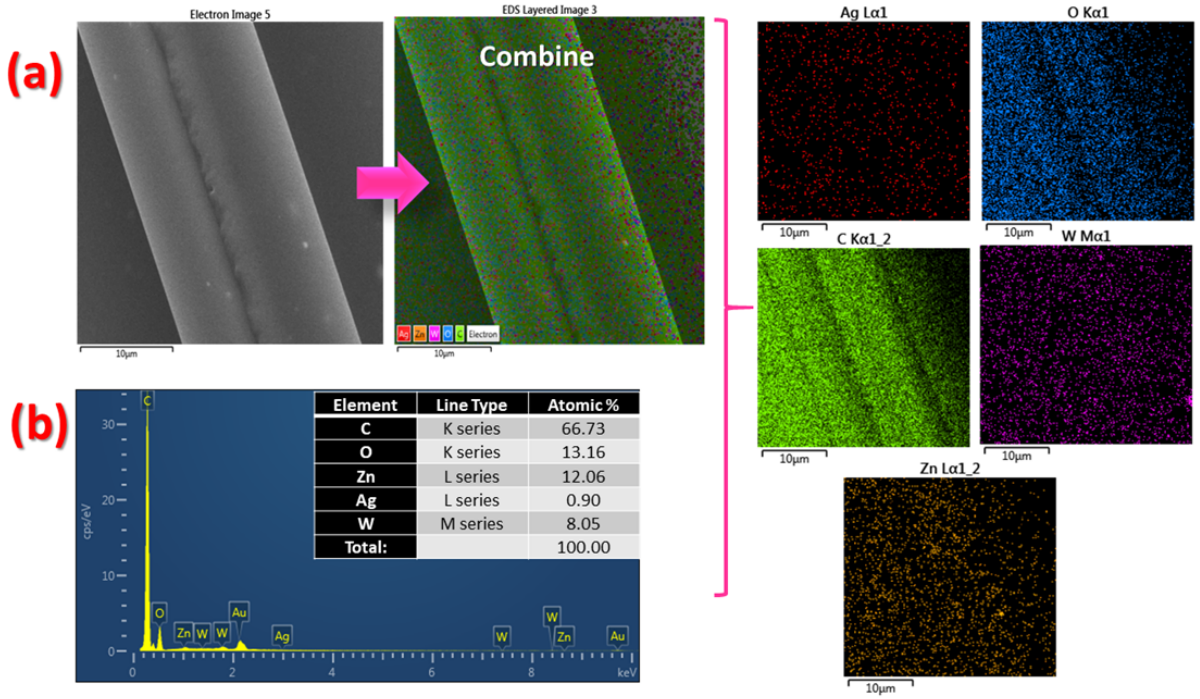

Figure 7. (a) FESEM image and corresponding combined elemental mapping of the $ZnWO_4$:Ag fibrous structure, showing homogeneous spatial distribution of the constituent elements. Individual elemental maps of Ag, O, C, W, and Zn confirm uniform dispersion along the fiber surface. (b) EDS spectrum and quantitative elemental analysis of the $ZnWO_4$:Ag fibers, confirming the presence of C, O, Zn, W, and Ag. Scale bar: 10 µm.

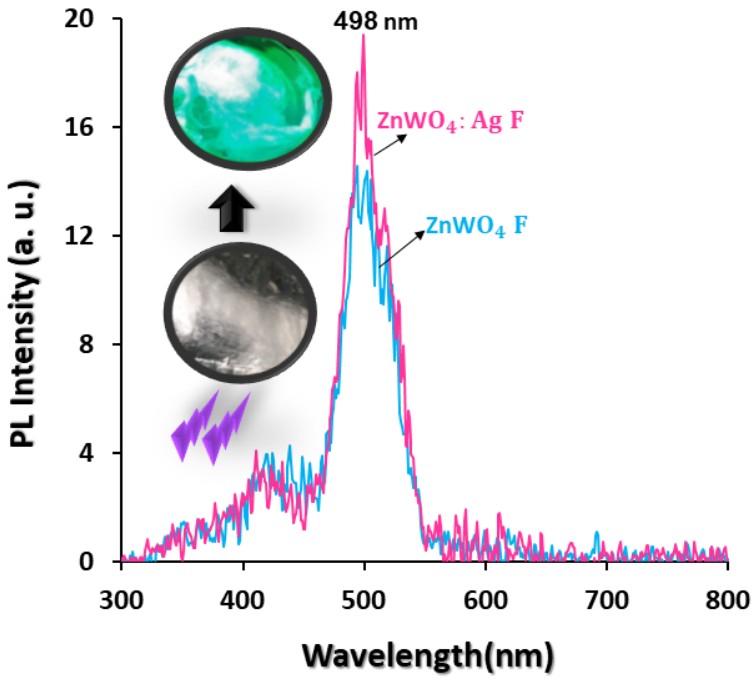

Figure 8. Photoluminescence (PL) emission spectra of pristine $ZnWO_4$ and Ag-doped $ZnWO_4$ powders under UV excitation, showing enhanced emission intensity upon Ag incorporation.

compared to the undoped counterpart, indicating that Ag incorporation plays a significant role in modifying the radiative recombination pathways.

The blue emission of $ZnWO_4$ is generally attributed to the radiative recombination of self-trapped excitons (STEs) localized within the $[WO_4]^{2-}$ tetrahedral groups of the crystal structure. In contrast, red emission components are associated with zinc vacancies (VZn) and Frenkel-type defects, which may arise from lattice distortions or defects related to W^{6+} ionic imperfections. Furthermore, the observed green emission is commonly linked to intrinsic structural defects in $ZnWO_4$ and is believed to originate from tunneling recombination processes between electron and hole centers. In this context, zinc vacancies and WO_3-related defects are considered as probable hole-trapping centers.

The enhanced PL intensity observed in the Ag-doped sample suggests that Ag ions and/or Ag-related defect states introduce additional radiative recombination centers or facilitate more efficient charge carrier trapping, thereby suppressing non-radiative recombination. These results demonstrate that Ag doping effectively tailors the optical emission behavior of $ZnWO_4$, making the material a promising candidate for luminescent, sensing, and radiation detection applications.

Ion beam induced luminescence (IBIL)

Ion Beam Induced Luminescence (IBIL) measurements were performed to investigate the luminescence response of the synthesized powders under proton irradiation and to further evaluate their potential for ionizing radiation detection (Fig. 9(a)). For this purpose, the samples were irradiated with a 2.2 MeV proton beam at a beam current of 4 nA, and the corresponding emission spectra were recorded.

As illustrated in Fig. 9(b), all investigated samples exhibit a dominant emission band centered at approximately 500 nm, located in the blue–green region of the visible spectrum. Among the samples, the Ag-doped $ZnWO_4$ fibers ($ZnWO_4$:Ag F) show the highest emission intensity, whereas the undoped $ZnWO_4$ fibers ($ZnWO_4$ F) display the weakest luminescence response. This trend is fully consistent with the photoluminescence (PL) results, confirming the beneficial role of Ag incorporation in enhancing the radiative recombination efficiency.

Compared to ultraviolet excitation (≈ 4.96 eV), the high-energy proton beam (2.2 MeV) generates a significantly larger population of excited charge carriers through ionization processes. Consequently, the emission intensities observed in the IBIL spectra are markedly higher than those recorded under UV excitation in PL measurements. This enhanced excitation efficiency highlights the strong interaction between energetic protons and the $ZnWO_4$-based lattice, leading to efficient generation of electron–hole pairs and subsequent radiative recombination.

The pronounced enhancement of ionoluminescence intensity in the Ag-doped fibers is attributed to the modification of the electronic structure induced by Ag ions, which introduces additional energy levels within the band gap of the $ZnWO_4$ host. These Ag-related states promote spectral overlap between the host band-gap emission and the electronic transitions of dopant-related states, facilitating efficient energy transfer processes. Such interactions effectively enhance the probability of radiative recombination and suppress non-radiative pathways, thereby improving the overall ionoluminescence performance. Overall, the IBIL

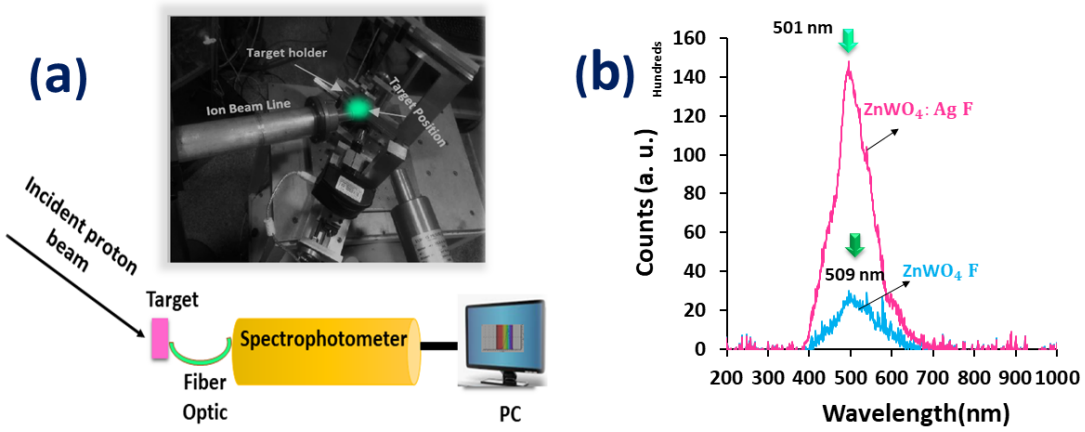

Figure 9. (a) Schematic representation of the ion beam induced luminescence (IBIL) experimental setup. (b) IBIL emission spectra of undoped $ZnWO_4$ fibers ($ZnWO_4$F) and Ag-doped $ZnWO_4$ fibers ($ZnWO_4$:Ag F) under 2.2 MeV proton irradiation, showing enhanced emission intensity for the Ag-doped sample.

results, in strong agreement with the PL findings, demonstrate that Ag doping significantly enhances the luminescent response of $ZnWO_4$ fibers under proton irradiation, confirming their promising potential for applications in ionizing radiation detection, scintillation materials, and advanced radiation-sensitive devices.

4. Conclusion

Ag-doped $ZnWO_4$ micro fibers were successfully synthesized using a facile and cost-effective drawing method, and their structural, morphological, and luminescent properties were comprehensively evaluated. XRD and Raman analyses confirmed the preservation of the monoclinic wolframite structure after Ag doping and fiber fabrication, while revealing controlled lattice distortion and reduced crystallinity that play a key role in tailoring the optical behavior. FESEM and EDS results demonstrated the formation of continuous fibrous structures with uniform surface decoration of Ag nanoparticles and excellent compositional homogeneity. Optical investigations showed a dominant blue–green emission around 500 nm, originating from self-trapped excitons and defect-related recombination centers within the $ZnWO_4$ lattice. Both PL and IBIL measurements revealed a pronounced enhancement of luminescence intensity upon Ag incorporation, with IBIL exhibiting significantly stronger emission due to the efficient generation of charge carriers under proton irradiation. The improved ionoluminescence performance is attributed to Ag-induced electronic states that facilitate energy transfer and suppress non-radiative recombination pathways. Overall, this work demonstrates, for the first time, the strong potential of $ZnWO_4$:Ag fibrous systems as flexible, radiation-responsive materials for scintillation, dosimetry, smart textiles, and optoelectronic sensing applications.

Acknowledgement: The authors thank Prof. Mohammad Hossein Majles Ara at Nanophysics Lab, Faculty of Physics, Kharazmi University, Tehran, Iran, for his valuable support in conducting the research and for the internal review and constructive feedback on the manuscript.

Authors Contribution
All authors contributed equally to the conception, design, execution, and writing of this work. All authors read and approved the final manuscript.

Availability of data and materials
The data that support the findings of this study are available from the corresponding author, upon reasonable request.

Conflict of interests
The authors declare that they have no known competing financial interests or personal relationships that could have appeared to influence the work reported in this paper.

References

[1] N. Enríquez-Sánchez, A. R. Vilchis-Nestor, S. Camacho-López, M. A. Camacho-López, and M. Camacho-López. Colloidal MnO_x NPs/carbon sheets nanocomposite synthesis by laser ablation in liquids. *Optics & Laser Technology*, **146**:107591, (2022). DOI: https://doi.org/10.1016/j.optlastec.2021.107591.

[2] S. Dey and A. K. Kar. Effect of acceptor concentration in the FRET-controlled photoluminescence of PMMA–ZnO nanocomposite for PLED applications. *Optics & Laser Technology*, **136**:106811, (2021). DOI: https://doi.org/10.1016/j.optlastec.2020.106811.

[3] S. Alamdari, M. Sasani Ghamsari, and M. J. Tafreshi. Novel scintillation properties by entrapping ZnO:Ga nanocrystals in epoxy polymer. . *Progress in Nuclear Energy*, **130**:103495, (2020). DOI: https://doi.org/10.1016/j.pnucene.2020.103495.

[4] A. S. Al-Hiti, A. H. H. Al-Masoodi, S. W. Harun, M. Yasin, and W. R. Wong. Tungsten trioxide (WO_3) film absorber for generating soliton mode-locked pulses in erbium laser. . *Optics & Laser Technology*, **8**:37, (2020). DOI: https://doi.org/, 131, 106429. https://doi.org/10.1016/j.optlastec.2020.106429.

[5] M. Hosseinpour, H. Abdoos, O. Mirzaee, and S. Alamdari. Fabrication and characterization of a new flexible ionizing ray sensor based on lead tungstate ($PbWO_4$). . *Ceramics International*, **49**:4722–4732, (2023). DOI: https://doi.org/10.1016/j.ceramint.2022.10.xxx.

[6] N. Heydarian Dehkordi, M. Raeisi, and S. Alamdari. Development of flexible scintillation sensors based on Ag- and Gd-doped $CdWO_4$ nanocomposites. . *Applied Radiation and Isotopes*, **189**:110457, (2022).
DOI: https://doi.org/10.1016/j.apradiso.2022.110457.

[7] S. Alamdari, M. H. Majles Ara, and M. J. Tafreshi. Synthesis and optical response of ZnO/$CdWO_4$:Ce nanocomposite with high-sensitivity detection of ionizing radiations. *Optics & Laser Technology*, **151**:107990, (2022).
DOI: https://doi.org/10.1016/j.optlastec.2022.107990.

[8] M. Hemmati, M. J. Tafreshi, M. H. Ehsani, and S. Alamdari. Highly sensitive and wide-range flexible sensor based on hybrid $BaWO_4$@CS nanocomposite. . . *Ceramics International*, **48**: 26508–26518, (2022).
DOI: https://doi.org/10.1016/j.ceramint.2022.06.xxx.

[9] X. Zhou, B. Xu, X. Zhao, H. Lv, D. Qiao, X. Peng, F. Shi, M. Chen, and Q. Hao. In situ growth method for large-area flexible perovskite nanocrystal films. . *Materials*, **17**:3550, (2024).
DOI: https://doi.org/10.3390/ma17143550.

[10] T. T. Guo, X. L. Yu, Y. H. Zhao, X. Y. Yuan, J. Y. Li, and L. X. Ren. Impact of spacer units on polymerization and self-assembly of bottlebrush block copolymers for photonic multilayer films. . *Macromolecules*, **53**:3602–3612, (2020).
DOI: https://doi.org/10.1021/acs.macromol.0c00234.